AGU PUBLICATIONS

JGR

Journal of Geophysical Research: Solid Earth

RESEARCH ARTICLE
10.1002/2014JB011060

Key Points:
- Reflected elastic waves can promote compaction band (CB) cascade formation
- Spatial CB distribution depends on layer geometry and material permeability
- CBs are more prone to develop in presence of intercalations of softer material

Correspondence to:
F. Cecinato,
francesco.cecinato@unitn.it

Citation:
Cecinato, F., and A. Gajo (2014), Dynamical effects during compaction band formation affecting their spatial periodicity, *J. Geophys. Res. Solid Earth*, *119*, 7487–7502, doi:10.1002/2014JB011060.

Received 20 FEB 2014
Accepted 5 SEP 2014
Accepted article online 8 SEP 2014
Published online 6 OCT 2014

Dynamical effects during compaction band formation affecting their spatial periodicity

Francesco Cecinato[1] and Alessandro Gajo[1]

[1]University of Trento, Department of Civil, Environmental and Mechanical Engineering, Trento, Italy

Abstract Compaction bands (CBs) are responsible for significant anisotropy alterations of permeability in geological materials; hence, understanding their formation conditions appears of key importance to all applications involving fluid extraction/injection from/into the ground. While most of the available models to understand CB formation are focused on interpreting the onset of a single CB, little effort has been so far dedicated to understand the documented periodicity of CBs. In this paper, the role of dynamical effects in inducing the post onset evolution of CBs is analyzed by means of a dedicated model for porous media with compressible constituents, with reference to a horizontal layer of sandy, water-saturated material. Elastic waves are generated as a first CB occurs due to sudden, localized volumetric collapse. If the waves are reflected at the interface with a softer material or with a previously formed CB, they produce significant local effective stress concentrations, which can promote the formation of further CBs in a cascade fashion, according to a regular geometric pattern. The spatial distribution of dynamically generated CBs, as well as the extent of the phenomenon, depends on the geometry of the domain and on the material's permeability. Sensitivity analysis is also performed to assess the key properties that promote dynamical CB in situ formation, identifying as the most influential conditions large stratum stiffness (increasing with depth) and the presence of softer layers. In contrast, the presence of less permeable and/or stiffer layers is not believed to play a major role in the proposed mechanism.

1. Introduction

Significant research interest in the geoscience community has been devoted over the last two decades to compaction bands (CBs), which constitute a particular form of localization of deformation. When subject to compressive stress states, some high-porosity materials give rise to nonuniform compaction into a series of subparallel, regularly spaced tabular zones, oriented approximately normal to the maximum principal stress. Such zones of compacted material are bound to directly affect the permeability of the material by changing both its pore volume and its pore structure [*Holcomb and Olsson*, 2003].

In general, compaction can occur in localized zones as a result of a combination of compaction and shear, within the broad definition of deformation bands [*Holcomb and Olsson*, 2003]. CBs constitute a limiting case of deformation bands where compaction occurs in the absence of macroscopic shear deformation [*Holcomb et al.*, 2007].

Since CBs cause significant permeability reduction relative to the uncompacted state, understanding their formation conditions and spatial distribution appears of paramount importance in all applications involving fluid extraction/injection from/into the ground (reservoir or aquifer production, CO_2, gas or hazardous waste geological storage, deep geothermal energy production, etc.). CBs are also associated with sand production during reservoir exploitation, as they have been found to occur as borehole breakouts, at the locations of maximum stress concentrations [*Haimson and Song*, 1998; *Olsson*, 1999; *Katsman et al.*, 2009]. Furthermore, the extensive occurrence of CBs during fluid production could enhance surface subsidence and therefore cause severe disturbance to the related industrial and civil activities.

Among the best documented field case studies of CBs are the Buckskin Gulch site in south central Utah [*Mollema and Antonellini*, 1996] and the Valley of Fire site in southern Nevada [*Sternolf*, 2006]. Both sites involve as favorable characteristics to CB formation the presence of coarse-grained, high-porosity sandstone [*Schultz*, 2009]. CB-genic (i.e., suitable to promote CB formation) material is generally reported to range from lightly cemented sandstone to essentially uncemented sands [*Holcomb et al.*, 2007].

CBs have also been reproduced in the laboratory, associated with stressed boreholes [*Haimson and Song*, 1998; *Katsman et al.*, 2009] or during triaxial compression tests [*Holcomb and Olsson*, 2003; *Baud et al.*,

2004] in sandstones, in mudstones [*Oka et al*., 2011], and in artificially or naturally cemented soils [*Castellanza et al*., 2009].

Compaction localization was first predicted to occur by *Rudnicki and Rice*'s [1975] strain localization theory, subsequently extended by *Issen and Rudnicki* [2000]. Among the main proposed collapse mechanisms are bond breakage [*Nova et al*., 2003], grain crushing [*Mollema and Antonellini*, 1996], pore collapse and pressure solution [*Lajtai*, 1974; *Fletcher and Pollard*, 1981; *Olsson*, 1999; *De Meer et al*., 2000].

While most of the available theoretical models to interpret the formation of CBs are focused on capturing the point of appearance of a single CB [e.g., see *Olsson*, 1999; *Holcomb and Olsson*, 2003], not many extensive studies have been dedicated to understand the documented spatial periodicity of occurrence of CBs. This aspect was recently brought to attention by *Regenauer-Lieb et al*. [2013], who proposed a rate-dependent model where the hydromechanical properties of the material and the velocity of deformation can be correlated with the periodicity of CBs. Further, *Stefanou and Sulem* [2014] discussed the thickness/periodicity of CBs in relation to material properties like grain crushability and hydraulic diffusivity. *Chemenda* [2009] showed, resorting to bifurcation analysis of compaction banding, that the ratio between CB thickness and spacing is related to all stress–strain parameters, with special reference to the hardening modulus.

In this work, a dynamical analysis is described that accounts for the generation and propagation of elastic waves as a first CB is formed in a fluid-saturated granular material. As soon as a CB abruptly appears in an otherwise homogeneous material, two main phenomena take place: (i) the pore water pressure is locally increased and diffused away as a function of the material permeability and (ii) two longitudinal elastic waves are produced on either sides of the domain, traveling at a speed that is a function of the material stiffness. Upon encountering an interface with a softer material or with an already formed CB, each elastic wave is partly transmitted further away and partly reflected. The reflected portion of the wave thus remains within the domain of interest, potentially giving rise to local stress concentrations, and subsequent further compaction localization (to which the material is prone, due to its homogeneity), as it collides with another wave traveling with opposite direction.

The analysis hereby proposed is based upon numerical simulations that were obtained by using an existing finite element formulation for analyzing the dynamic conditions of saturated porous media at large strains with compressible solid and fluid constituents [*Gajo and Denzer*, 2011]. This study is relevant to a post inception analysis that disregards the conditions under which a first CB is generated; it aims at proposing a physical interpretation for the in situ spatial periodicity of subsequently formed CBs, after a first CB occurrence, according to a pattern that appears to be regulated by the geometry of the considered domain and by the material properties.

2. Model Formulation

The mathematical model that was employed for the dynamic analysis of CB formation is an extension of the small strain theory for wave propagation in saturated porous media by *Biot* [1941, 1956, 1962a, 1962b, 1973]. Since the occurrence of CBs typically involves localized large strains, the formulation by *Gajo and Denzer* [2011] was adopted, which builds upon Biot's theory providing the theoretical framework and the finite element implementation for dynamic analyses within a hyperelastic framework [*Gajo*, 2010] for saturated porous media with compressible constituents subjected to finite strains. The adoption of an elastic framework to model a problem involving inelastic deformation is a simplification, already adopted by other authors in similar contexts [e.g., see *Sternlof et al*., 2005], justified by the fact that after the onset of a CB, typically plastic deformation occurs solely within the band while the rest of the domain undergoes elastic unloading [*Rice and Rudnicki*, 1980, *Chemenda*, 2009]. Further explanation of this assumption is provided by the main analysis results, discussed in section 3.

Gajo and Denzer's [2011] model fully takes into account all nonlinear geometrical terms featuring in the porous medium, i.e., both in the solid skeleton and in the fluid and solid constituents. The reliability of this approach has been verified in a number of numerical tests, where the finite element solution in both 1-D and 2-D elastic wave propagation problems in saturated porous media was successfully compared with available analytical solutions [*Gajo and Denzer*, 2011].

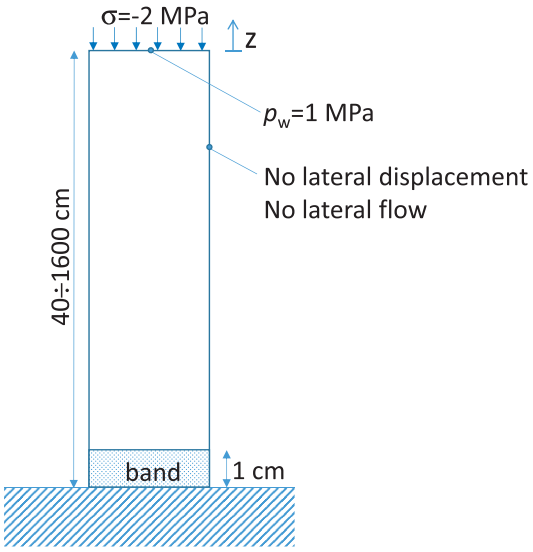

Figure 1. Schematic of the 1-D problem. By symmetry, only one half of the domain is described. At the bottom boundary (midplane of CB), neither fluid flow nor vertical displacement are permitted.

The balance equations of *Gajo and Denzer* [2011], written for a porous medium saturated by a single fluid component, at large strains, are outlined in sections A1–A3.

3. Dynamical Effects in the CB Formation

The dynamic analysis was carried out considering a reference horizontal layer of granular (sandy) material subject to a homogeneous stress state. The onset of a first appearing CB was simulated by imposing an abrupt (in a total time in the range of 15–45 μs) decrease of elastic stiffness within a thin layer of 2 cm thickness in an otherwise homogeneous, larger domain. In fact, in the early times of CB formation, the collapsing zone experiences major grain rearrangement causing a temporary drop of tangent stiffness, as shown by the typical "shelf" zone, occurring at CB formation in the stress–strain curve obtained in the laboratory [e.g., see *Issen and Rudnicki*, 2000, Figure 4]. In the first instants, the solid skeleton is starting to collapse; however, no significant deformation occurs before pore water flows out of the CB area. Thus, the very initial phases (of the order of tenths of milliseconds from CB initiation) of CB formation are characterized by large pore pressure and small volumetric deformation. In subsequent times (lasting some tenths of second, widely varying depending on the material permeability), as the pore water pressure gradually diffuses away, intergranular contacts in the CB zone are recovered and material stiffness progressively becomes larger as large volumetric strain occur. Upon completion of excess pore pressure dissipation, the CB stiffness becomes larger than the initial one, as tighter particle packing compared to the undisturbed state is achieved.

The 3-D problem of elastic wave propagation within a horizontal geological layer, consequent to the formation of an indefinitely extended CB perpendicular to the vertical (overburden) stress, was simplified for symmetry reasons to the 1-D geometry represented in Figure 1. This one-dimensionality assumption, implying the instantaneous CB formation over a large lateral extent, is justified by the above stated hypothesis of homogeneity of material and of stress state and was often used in the literature [e.g., *Rudnicki and Rice*, 1975].

Symmetry allowed us to simplify the geometry by describing only one half of the domain, considering a semithickness lying in the range 40–1600 cm and the CB having 1 cm semithickness as it forms at one edge (where the symmetry plane is located) of the domain. As boundary conditions, to enforce 1-D assumptions neither lateral displacement nor fluid flow was allowed at the lateral boundaries. At the bottom, neither vertical displacement nor fluid flow was permitted and at the top a constant total overburden vertical stress of $\sigma = -2$ MPa (compressive stress is here taken negative) and a pore pressure of $p_w = 1$ MPa (corresponding to a depth of about 100 m) were imposed. As initial conditions, a stress state in equilibrium with the stress applied at the top boundary was assumed.

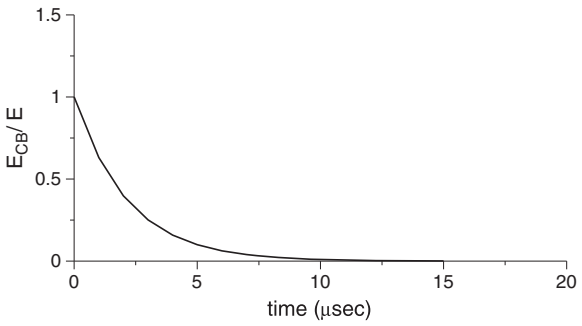

Figure 2. Stiffness decay function within the CB from the undisturbed value E to the final value E_{CB} to reproduce in a simplified manner the sudden drop of tangent stiffness occurring at CB onset. In this case $E_{CB}/E = 0.001$ and stiffness decay time $\Delta t = 15$ μs.

The above settings aim at reproducing averagely representative conditions for the

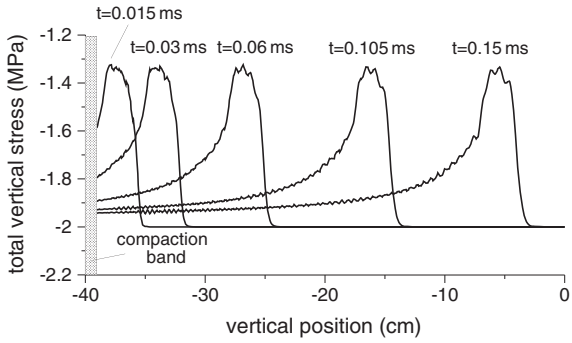

Figure 3. Simulation of elastic wave transmission through a 40 cm semithickness domain of granular material with hydraulic conductivity $K_D^0 = 10^{-5}$ m/s ($\kappa = 1$ darcy) in terms of total vertical stress. The different curves represent different times after CB initiation in the time range 0–0.15 ms.

formation of CBs in nature, in uncemented sandy materials. In fact, field evidence related to compaction localization generally shows that CBs typically form in lightly cemented or uncemented sandy materials, subjected to a vertical overburden ranging from a few MPa to 30 MPa and to pore pressures of less than 13 MPa, at undisturbed (initial) porosities of $n_0 = 10$–25% [*Holcomb et al.*, 2007], and permeability κ between 2 and 20 darcies (i.e., saturated hydraulic conductivities in the range $K_D^0 = 2{\cdot}10^{-5} - 2{\cdot}10^{-4}$ m/s) [e.g., *Fossen et al.*, 2011]. CBs' thicknesses are typically less than 1.5 cm [*Holcomb et al.*, 2007; *Stefanou and Sulem*, 2014] and the CB formation can bring about in highly porous materials a porosity reduction of 10% to 20% [*Olsson*, 2001; *Klein et al.*, 2001; *Holcomb et al.*, 2007], corresponding to a volumetric deformation larger than 10%, relative to the surrounding uncompacted material.

An elastic stiffness of $E = 5000$ MPa was assumed for the material in the bulk of our analyses, corresponding to a depth of the order of 1000 m for an uncemented material (calculated after *Hardin and Black* [1968] considering an effective mean stress of 10 MPa), or to a lower depth for a weakly cemented material. Stiffness was abruptly (in 15 μs) reduced to $E_{CB} = 5$ MPa within the CB zone to reproduce localized collapse. Since our interest was focused on dynamic conditions, a rigorous analysis of postlocalization regime was not attempted. However, imposing a sudden elastic stiffness decrease can be considered a representative simplification of the first instants of postcritical regime, when grain rearrangement causes the CB zone to exhibit temporary softening, during the time needed for consolidation to occur.

The value of ratio $E_{CB}/E = 0.001$ results from finite strain calculations, assuming a volumetric strain within the CB of about 10%. To reproduce this collapse effect, the stiffness decay function of Figure 2 was employed for the bulk of our analyses (see section 5 for model sensitivity to this assumption).

In most of the numerical analyses hereby presented, the node spacing in the finite element mesh was taken equal to 1 mm. For the larger domain cases, the 1 mm node spacing was adopted only within the CB area, while it was gradually increased outside, proportionally to the distance from the CB, to minimize computational time while keeping a representative discretization of the domain. Mesh dependency was investigated by means of numerical experimentation, to ensure that the highest wave frequencies were adequately represented by the mesh spacing.

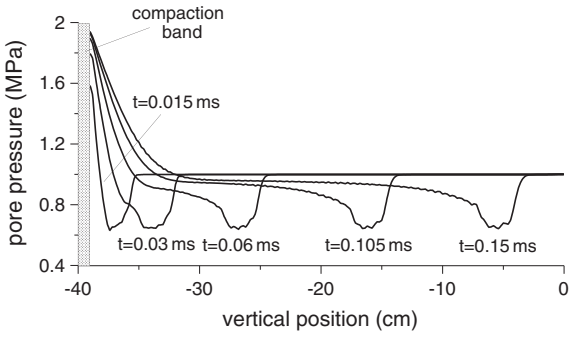

Figure 4. Simulation of elastic wave transmission through a 40 cm semithickness domain of granular material with hydraulic conductivity $K_D^0 = 10^{-5}$ m/s ($\kappa = 1$ darcy) in terms of pore pressure. The different curves represent different times after CB initiation in the time range 0–0.15 ms.

In Table A1, all relevant parameters adopted in our calculations are reported. In Figures 3 and 4 simulation results are shown for a 40 cm semithickness domain of granular material with hydraulic conductivity $K_D^0 = 10^{-5}$ m/s ($\kappa = 1$ darcy), in terms of total stress and pore pressure, respectively. It can be observed that the sudden stiffness drop occurring at CB onset induces the propagation of a longitudinal wave of the first type [e.g., see *Biot*, 1956], which is represented at different time instants as it travels across the domain (at velocity $v_I = 2361$ m/s), for a total time range of 0–0.15 ms. The elastic wave propagation in the domain is associated with a decrease of both total stress σ (in absolute value) and of pore pressure p_w. Within the CB area, however, pore pressure increases so

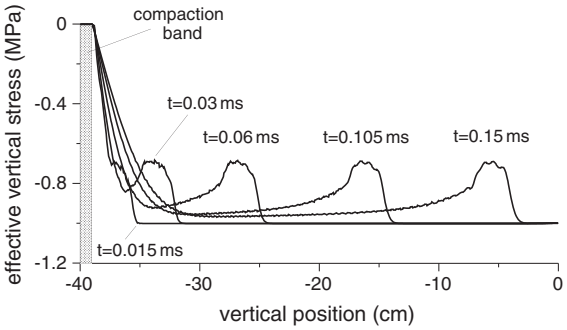

Figure 5. Simulation of elastic wave transmission through a 40 cm semithickness domain of granular material with hydraulic conductivity $K_D^0 = 10^{-5}$ m/s ($\kappa = 1$ darcy) in terms of effective vertical stress. The different curves represent different times after CB initiation in the time range 0–0.15 ms.

much, during the first fractions of second following the CB formation, that effective stress σ' (expressed as $\sigma + p_w$) is virtually vanished. This can be observed in Figure 5, where the same simulation results described above are expressed in terms of effective stress: in the whole CB area, $\sigma' = 0$.

Also, the areas of the domain that are close to the CB exhibit, at early times, a dramatic effective stress decrease. The spatial extent of the practically null effective stress zone around the CB depends upon the pore pressure diffusion, which in turn is governed by the material's permeability. In Figures 6 and 7, where the hydraulic conductivity is respectively set to $K_D^0 = 10^{-4}$ m/s ($\kappa = 10$ darcies) and $K_D^0 = 10^{-6}$ m/s ($\kappa = 0.1$ darcy), the effects of permeability on the results obtained for the reference material are explored. The different curves represent different times after CB initiation. In the larger permeability case (Figure 6), the propagation of longitudinal waves of the second type [e.g., see *Bourbié et al.*, 1987], of velocity $v_{II} = 850$ m/s, can be observed along with those of the first type. In contrast, adopting lower permeability values (Figures 5 and 7) results in the complete damping of the waves of the second type.

For decreasing permeability, all other things being equal, outside of the CB effective stress tends to decrease only in correspondence of the longitudinal wave of the first kind, while it remains virtually equal to the undisturbed value ($\sigma + p_w = -1$ MPa) elsewhere in the domain. In fact, the shape of the effective stress distribution reflects the capability of excess pore pressure to diffuse away: at the same instant, the smaller permeability is, the sharper (i.e., more localized in space) will be the spike carrying an effective stress decrease. It is worth adding that in section 5 the implications of the principal assumptions mentioned above are explored in detail.

In Figure 8, pore pressure dissipation profiles are plotted for a larger domain (sandy layer of 16 m semithickness), with elastic stiffness $E = 5000$ MPa and hydraulic conductivity $K_D^0 = 10^{-4}$ m/s ($\kappa = 10$ darcies). For this permeability, the average time needed for excess pore pressure dissipation lies in the order of a second. The dashed lines denote early times after the CB formation, when the elastic wave is propagating through the domain (the band thickness is out of scale). The solid lines represent later instants, when the elastic wave has already exited the domain and only pore pressure diffusion occurs.

In Figure 9 the reflection and transmission of an elastic wave caused by a CB are analyzed, at the incidence (a) with the interface between two porous media having very different stiffness ($E_1 = 5000$ MPa, $E_2 = E_1/10, K_{D1}^0 = K_{D2}^0 = 10^{-5}$, m/s or $\kappa = 1$ darcy) and (b) with a recently formed CB. The latter case corresponds to a situation where the elastic wave triggered by a just formed CB (#2, at the left boundary of the domain) travels through a previously formed CB (#1, in the middle of the domain) where volumetric collapse occurred in the very recent past, so that excess pore pressure is still large in its neighborhood. To analyze this situation, implying for CB #1 a dramatic stiffness decrease and pore pressure increase, a special simulation setup was necessary. The problem was split in two simulations, namely, (i) the formation of CB #1 alone and (ii) the simultaneous formation of CB #1 and CB #2. Then, the approximate linearity of the problem enabled us to apply the

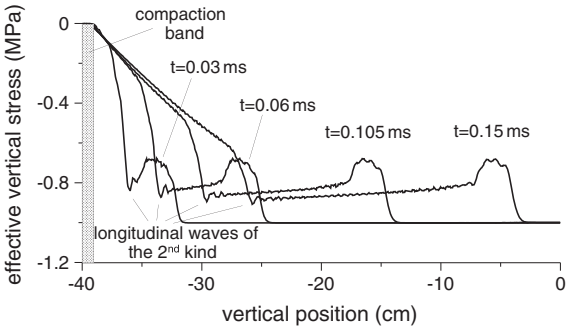

Figure 6. Simulation of elastic wave transmission through a 40 cm semithickness domain of granular material with hydraulic conductivity $K_D^0 = 10^{-4}$ m/s ($\kappa = 10$ darcies) in terms of effective vertical stress. The different curves represent different times after CB initiation in the time range 0–0.15 ms.

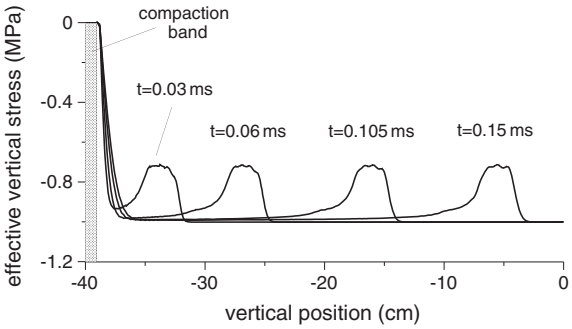

Figure 7. Simulation of elastic wave transmission through a 40 cm semithickness domain of granular material with hydraulic conductivity $K_D^0 = 10^{-6}$ m/s ($\kappa = 0.1$ darcy) in terms of effective vertical stress. The different curves represent different times after CB initiation in the time range 0–0.15 ms.

superposition principle, so that the ultimate result (shown in Figure 9b) is the difference of results of simulation (ii) minus simulation (i). As a result, stiffness within the CB is abruptly reduced from the undisturbed value of $E_1 = 5000$ MPa to $E_{CB} = 5$ MPa, whereas the pore pressure is still very large within the bands. Thus, the volumetric deformations within the band are regulated by the consolidation process.

It can be observed that in both cases of Figures 9a and 9b, the reflected wave induces an effective stress increase (in absolute value) of the order of 3–5%.

It can be argued that when two elastic waves traveling with opposite direction after being reflected by a boundary separating the intact material from a softer one, or from a recently formed CB, collide, by superposition they could bring about a local increase of effective stress of the order of 6–10% (within the parameter range considered in this work). Due to the assumption of homogeneity of both the material and the stress state, the whole soil layer is very close to the boundary of the domain of "strong ellipticity" [e.g., see *Bigoni and Zaccaria*, 1992]; hence, it is prone to develop localized collapse. Consequently, a local increase of effective stress as the one caused by wave collision might induce the formation of a further CB at the position where the two waves encounter.

The outcomes of the dynamic analysis described above provide further justification for treating the problem at hand in the framework of elasticity: elastic unloading, due to a decrease of effective vertical stress, is predicted to take place in the bulk of the domain both at very early times (i.e., associated with the initial wave propagation) and at later times (i.e., during the pore pressure dissipation process), with the sole exception of the collision point of two opposite waves, where a subsequent CB can occur as a result of localized effective stress increase.

From the energetic point of view, it is worth noting that energy dissipation is associated with the plastic work of deformation within the CB, which is reproduced in our framework in a simplified manner with a stiffness decrease. On the other hand, energy dissipation due to water viscosity is neglected, due to the basic assumption of isothermal conditions. Of the total deformation energy E_{tot} involved in CB formation, which can be calculated knowing the effective stress and the final volumetric strain within the band, only a small part E_w is carried by the elastic wave generated upon CB formation. As an example, with reference to parameter settings of Figure 5, by performing a time integral of the power per unit area carried by the wave, we obtain that E_w is less than 1% of E_{tot}.

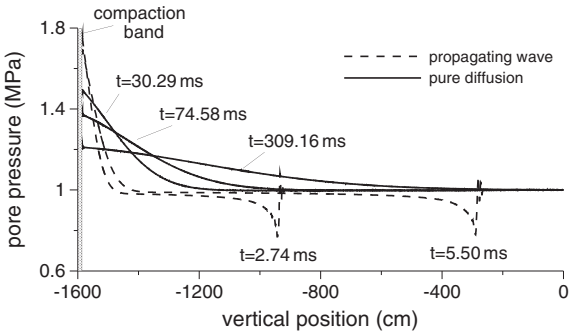

Figure 8. Pore pressure dissipation profiles for a 1600 cm semithickness domain with hydraulic conductivity $K_D^0 = 10^{-4}$ m/s ($\kappa = 10$ darcies). The different curves represent different times after CB initiation in the time range 0–310 ms. The dashed lines denote early times, when the elastic wave is propagating through the domain, while the solid lines represent later instants, when only pore pressure diffusion occurs.

It can be finally observed that the present analysis is limited to the first moments after a first CB occurrence, when the large deformation associated with pore volume collapse has not yet had the time to develop. Hence, despite our adoption of a large-strain approach ensures our accuracy of calculation, also a small strain analysis could have arguably led to similar results.

4. Dynamically Induced CB Periodicity

Within the framework described above, the formation of a first CB at any point in the domain (for any reason, e.g., the existence of a

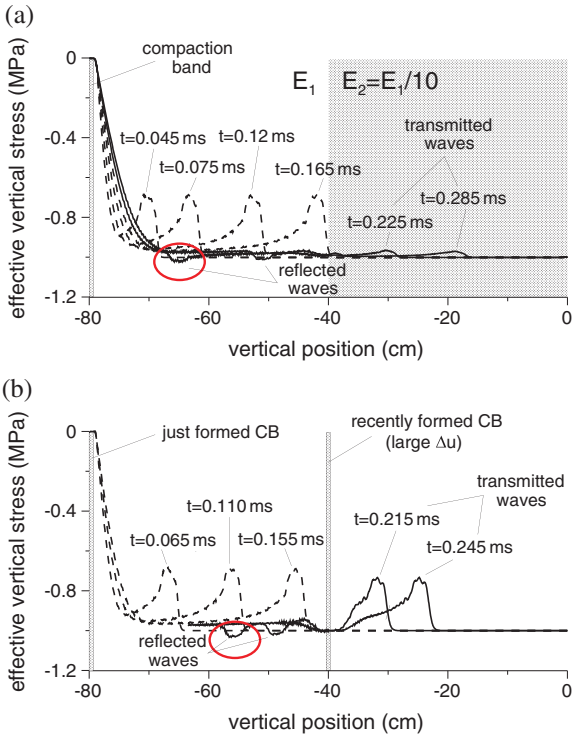

Figure 9. Simulation of elastic wave transmission and reflection at the interface with (a) a softer material with $E_2 = E_1/10$ and (b) a very recently formed CB, characterized by large excess pore pressure and a large temporary stiffness drop. The different curves represent different times after CB initiation, of which dashed lines represent times preceding the interface encounter and solid lines represent times following the interface encounter.

local structural weakness) can induce, in a cascade fashion, the formation of additional subsequent CBs where the induced elastic waves collide with each other, according to a regular geometric pattern.

The mechanism of recurring, subsequent strain localization is envisioned to take place in a similar fashion to that described by *Gajo et al.* [2004] for drained, quasi-static conditions. After the formation of a first localization band, elastic unloading and plastic loading occur, respectively, outside and inside the band. Shortly afterward, the so-called "band saturation" is reached, bringing the material outside the band again on the boundary of the domain of "strong ellipticity". Hence, subsequent band formation is likely in another location of the domain upon the occurrence of a small perturbation, as the one brought about by a collision of reflected waves.

In Figure 10, a schematic shows the possible mechanism of CB formation at different time instants, in a 1-D domain of initially homogeneous material bounded at both sides by a softer material (this leads to CB-genic wave reflections, as discussed above, contrary to the case of encountering stiffer boundaries, as discussed in section 5). The vertical position (i.e., depth) corresponds to the horizontal axis in the figure. At the onset of a first band (Figure 10a), for instance in a position located at a distance L from the left boundary, two longitudinal elastic waves are generated traveling on either side of the band, until they are (partly) reflected as they encounter the interface with the softer material at the domain boundary. The leftward traveling wave is first partly transmitted, partly reflected upon meeting the left boundary, and subsequently partly transmitted, partly reflected as it comes across the just formed CB. The rightward traveling wave will obviously need more time to reach the boundary, with the given geometry. If the total length of the considered domain is $\alpha \cdot L$ (with $\alpha > 1$), there will be a collision of the two opposing reflected waves after a time $\Delta T_1 = \alpha L/v$ (where v the wave velocity) since the first band generation, at a symmetric location with respect to the first band, i.e., at a distance L from the right boundary. At this moment, a second CB is formed which will in turn generate two further longitudinal elastic waves (Figure 10b), while the partly reflected portions of the waves generated from the first CB will keep traveling within the domain, with fading energy levels. By following the paths of the two newly formed waves, the next collision point can be predicted after a time $\Delta T_2 = (\alpha L - L)/v$ since the second band generation, at a distance $2L$ from the left boundary, i.e., at a distance L to the right from the first CB. At this point, a third CB is formed and the process will continue along the same lines, forming a fourth CB after a time $\Delta T_3 = (\alpha L - 2L)/v$ since the third band generation, at a distance $2L$ from the right boundary, a fifth CB after a time $\Delta T_4 = (\alpha L - 3L)/v$ since the third band generation (Figure 10c), and so forth in a cascade fashion. Every further (ith) CB will thus occur after a time ΔT_i that is shorter by L/v compared to the previous occurrence time ΔT_{i-1}. It should be noted that the time needed for the formation of each CB is here considered negligible compared to the time scale of elastic wave propagation within the domain; hence, the generation of every new elastic impulse is considered to occur with no delay with respect to each wave collision instant. This assumption corresponds to instantaneous CB formation over large planar areas, in light of the material and stress homogeneity assumptions stated in section 3. In general, the presence of inhomogeneities might give rise to deformation bands progressively propagating along a plane. Since the velocity of propagation of strain localization in

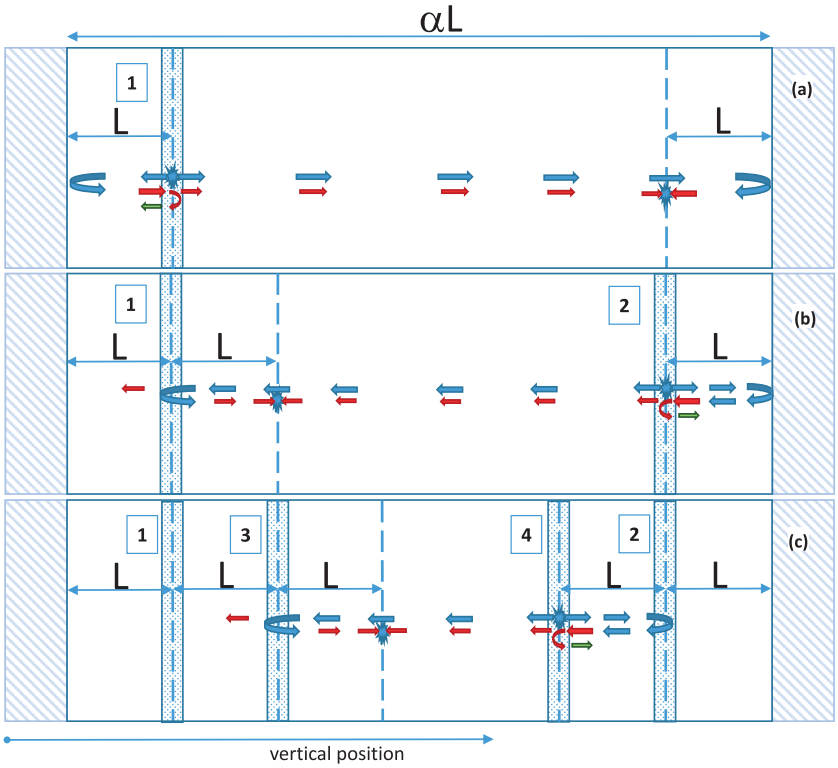

Figure 10. Schematic of the cascade CB formation mechanism in a homogeneous material bounded at both sides by a softer material. Considering that the first CB forms at time $T_1 = 0$, scheme (a) shows a snapshot at $T_2 = \alpha L/v$, when the second CB is just forming, (b) shows the instant $T_3 = T_2 + (\alpha L - L)/v$ when the third CB is just forming, and (c) shows the onset of the fifth CB at $T_5 = T_4 + (\alpha L - 3L)/v$, where $T_4 = T_3 + (\alpha L - 2L)/v$.

saturated porous media is unknown, it cannot be excluded that the progressive CB lateral propagation may occur with comparable velocity to that of wave propagation. In such cases, nonplanar longitudinal waves might be generated; hence, our analysis would not be applicable.

4.1. Suitable and Unsuitable Conditions for Cascade CB Formation

With reference to the situation illustrated in Figure 10, it should be observed that CBs subsequent to the first one can form only at some distance from the already formed CBs; i.e., CBs can form only at places where the excess pore pressure Δp_w is sufficiently small or zero. Only in these areas the effective stress level remains close to the undisturbed value ($\sigma' = \sigma + p_w = 1$ MPa in the examples of Figures 3–9), so that any wave collision occurring there can bring about a sufficiently large overstress $\Delta\sigma'$ (of the order of 6–10%, as discussed in section 3) to trigger localized compaction. For this reason, CBs cannot occur too close to each other, and their cascade formation will stop eventually, depending on the domain geometry and on the material permeability (unless, at a future time, another cascade CB formation is triggered by a new "first CB" occurrence). In other words, within the domain of interest there will be some CB-genic elastic wave collisions, while other collisions will fail to promote any localized volumetric collapse. To better illustrate the above discussed mechanism, in Figure 11 a situation of "unfruitful wave collision" is shown: as an example, the elastic waves generated from the second CB of Figure 10 are tracked. The initially rightward traveling wave W1 is first reflected at the right boundary, then transmitted through the second CB (hereafter called W1RT), while the initially leftward traveling wave W2 is partly reflected (W2R) and partly transmitted (W2T) at the first CB location. The reflected part W2R collides with W1RT after a time $\Delta T = (\alpha L - L)/v$ since the second band generation, at a distance $2L$ from the left boundary, forming a third CB. At the same time, the transmitted part W2T is further reflected at the left boundary (becoming W2TR). Two additional elastic waves (W3 and W4) are generated upon formation of the third compaction band, the leftward of which (W4) will collide with W2TR after a time $\Delta T = \alpha L/v$. The latter collision, however, fails to trigger any localized deformation as it occurs exactly in correspondence with a recently formed CB, where pore pressure is large and consequently the effective stress is small.

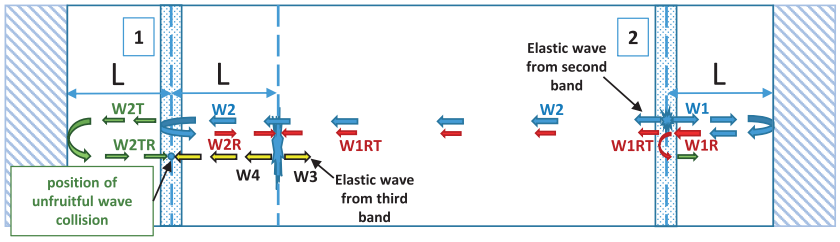

Figure 11. Schematic of a case of "unfruitful wave collision" in a homogeneous material bounded at both sides by a softer material. Along the lines of Figure 10, the third CB is shown as it forms at $T_3 = T_2 + (\alpha L - L)/v$, causing two further waves, W3 and W4. The collision between waves W4 and W2TR, occurring at $T = T_2 + \alpha L/v$, fails to trigger localized deformation as it occurs in correspondence with a very recent CB, where effective stress is small.

Not only collisions occurring in correspondence with a recently formed CB but also those occurring in the recent CB's surroundings might fail to promote further compaction. In fact, as could be observed in Figures 5–7, a transient effective stress reduction due to pore pressure rise will occur not only within the CB thickness but also in a neighborhood of the band location. Such neighborhood will be more or less wide, at a given instant, depending on the material diffusive properties. Hence, the minimum distance from a recently formed CB where another elastic wave collision can be fruitful (i.e., the minimum CB spacing) is expected to be a function of permeability. This is in line with earlier findings, as *Regenauer-Lieb et al.* [2013] and *Stefanou and Sulem* [2014] identified permeability as a parameter that controls the periodicity and/or thickness of CBs.

The above described mechanism thus explains why the subsequent wave reflections do not lead to induce CBs everywhere within the homogeneous soil layer and tend to stop as a minimum spacing is attained. It is worth remarking that only the first reflected waves are considered in the analysis, because successive reflections are associated with further losses of energy, leading to increasingly weaker effects in the local effective stress state.

4.2. Influence of Domain Geometry on the CB Pattern

The influence of the domain geometry on the CB formation pattern mainly lies in the above introduced parameter α, representing the ratio of the total domain length to the distance L. In general, the larger α is, the larger the number of CBs that can form. With reference to the geometry of Figure 10, it can be inferred that if α is an integer number, the maximum theoretical number of CBs that can be formed with the above described elastic wave collision mechanism is equal to $\alpha - 1$, with a perfectly homogeneous distribution across the domain. If instead α is a rational number, less even CB distributions are possible. Figures 12 and 13 show some sample theoretical CB patterns as a function of the domain geometry. When α is a rational

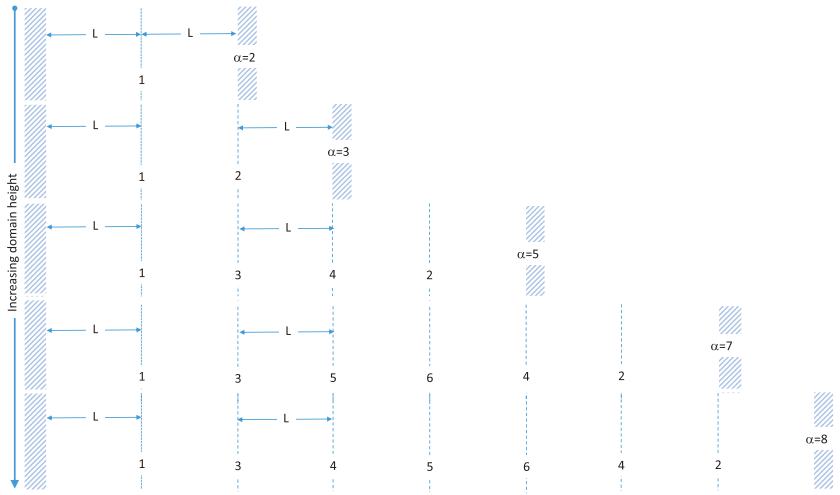

Figure 12. Sample theoretical CB spatial patterns when α is an integer number.

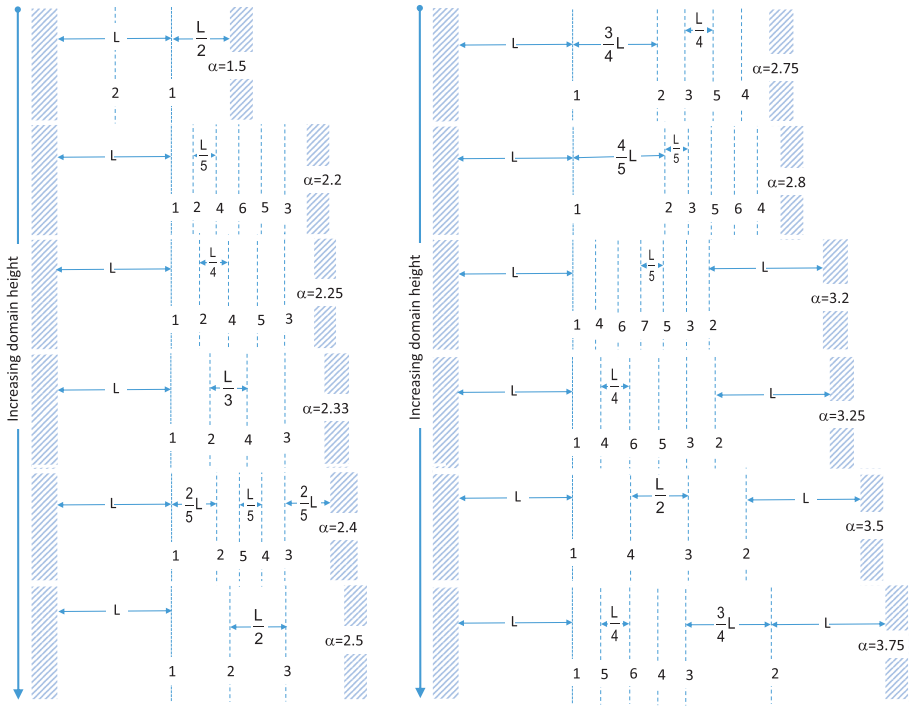

Figure 13. Sample theoretical CB spatial patterns when α is a rational number.

number, the CB formation pattern will be (i) centrally symmetric, if the integer part of α is an odd number and its decimal part is smaller or equal to 0.5, and (ii) asymmetric otherwise. Moreover, the former case corresponds to a spatial concentration of CBs in the middle part of the domain, i.e., a group of more finely spaced CBs will develop, with spacing βL, located at a distance L from either boundary of the domain. In this case factor β will be equal to the decimal part of α.

It should be remarked that the above discussed effects of geometry on the CB spacing are expected to be secondary to the effects of permeability, as the development of the theoretical geometrical pattern will be arrested as soon as the local excess pore pressure will prevent the development of a sufficient overstress to trigger localized compaction.

Within the above presented framework, it is plausible that different CB families form in different periods, successively refining the resulting overall CB spacing of a domain, or increasing the thickness of existing compacted zones. In fact, when all elastic waves have faded and the excess pore pressure within each CB zone is eventually dissipated, the boundary effective stress regime is restored everywhere in the domain, and existing CBs constitute zones of decreased permeability and increased stiffness. Due to a potential future insurgence of a "new" CB, an analogous cascade formation mechanism can occur. However, the presence of historic CBs may locally alter the excess pore pressure diffusion pattern, thus most likely affecting the spatial pattern of subsequent CBs. On the other hand, as shown in section 5, the location of a historic CB (where excess pore pressure does not any longer exist) does not constitute a fruitful reflection point for waves generated by other CBs.

5. Sensitivity Analysis and Discussion

To explore more systematically the effect of the key factors involved in this study on the dynamical CB formation mechanism, further simulations are discussed hereafter focusing on assessing the model sensitivity to the different parameters involved.

The influence of elastic stiffness on the likelihood of inducing subsequent CBs was explored (the figure is not shown here for the sake of brevity), with reference to the schematic of Figure 9a (where the stiffness change is set to $E_2 = E_1/10$), by keeping the same permeability for the two materials and evaluating the results for the

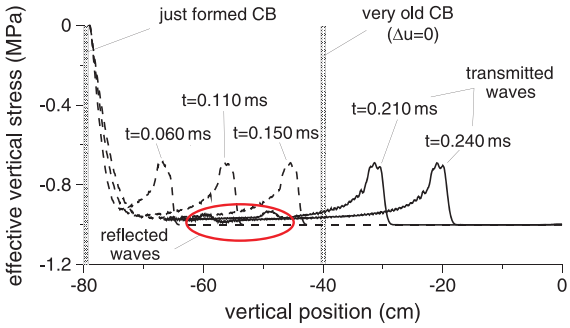

Figure 14. Simulation of elastic wave transmission and reflection at the interface with a very old CB, within which no excess pore pressure exists and stiffness is increased by a factor of 1.3 compared to the undisturbed value, as a result of pore space reduction. The different curves represent different times after CB initiation, of which dashed lines represent times preceding the interface encounter and solid lines represent times following the interface encounter. Contrary to what is shown in Figure 9b, in this case the reflected waves do not carry a net effective stress increase, but a small decrease.

cases of $E_2 = E_1/2$ and $E_2 = E_1/100$. It emerges that the amplitude of the reflected wave, i.e., the local effective stress increase, is an increasing function of ratio E_1/E_2. However, such increase is less than linear, so that the wave amplitude increase between case $E_1/E_2 = 2$ and case $E_1/E_2 = 10$ is considerably larger than that between case $E_1/E_2 = 10$ and $E_1/E_2 = 100$. Hence, the presence in situ of one or more intercalations of softer materials within an otherwise stiffer sandy material is a key factor to promote CB cascade formation according to a regular pattern. Anyway, the stiffness discontinuity at the interface between the two materials need not be unrealistically large for dynamical effects to be effective.

To assess the relative importance of permeability changes compared to stiffness changes, with reference to the schematic of Figure 9a, different cases were examined keeping the same stiffness in the two materials ($E_1 = E_2 = 5000$ MPa) but varying the permeability of the second material ($K^0_{D2} = (0.01 - 10)K^0_{D1}$). Regardless of whether the permeability of the second material is set to 1 or 2 orders of magnitude smaller or larger than that of the first material, no appreciable wave reflection occurs at the interface. This is consistent with theoretical expectations concerning wave propagation in saturated porous media. High-frequency components, involving relative motion between the two (solid and liquid) phases, are the fastest and shortest reaching (i.e., most heavily damped) compared to the low-frequency components (implying the absence of relative motion between the phases). For a given permeability, it is possible to theoretically predict the threshold travel distance beyond which only the low-frequency components can propagate [*Gajo*, 1995]. Within the permeability range investigated here, the threshold distance is of the order of 1–10 cm. Thus, approaching the interface between the two materials (located, in the example of Figure 9a, 40 cm from the origin), the wave mostly consists of the low-frequency components, which travel undisturbed across the interface without any reflection. In fact, the formation of reflected waves is, in general, caused by some type of discontinuity of material or hydraulic properties at the boundary between two media. While a stiffness discontinuity (discussed above) does represent a disturbance in the solid phase, a permeability change would alter the wave propagation mode only if high-frequency components still existed.

In summary, it could be inferred that a permeability range exists within which geologic materials are prone to develop cascade CB formation. On the one hand, permeability should not be exceedingly large, or the pore pressure dissipation profiles would be too wide (cf. Figure 6) to enable the local effective stress increase to trigger subsequent CBs. On the other hand, permeability should not be too small, as this identifies fine-grained, low-porosity materials (e.g., clay and claystone) which have been shown in the literature to be unsuitable for the onset of a first CB.

While Figure 9b shows the effect of the incidence of elastic waves at the interface with a recently formed CB (hence still affected by large excess pore pressure, induced by the loosening of intergranular contacts and grain rearrangement, associated with localized collapse), in Figure 14 the situation is depicted when elastic waves meet a historic (very old) CB, represented by a 1 cm thick layer of compacted material. In uncemented materials, an old CB zone is expected to be stiffer, due to increased grain interlocking and decreased porosity, compared to the undisturbed material. Within the historic CB, no excess pore pressure applies, and elastic stiffness is set to $E_2 = 1.3 \cdot E_1$ (calculated after *Hardin and Black* [1968] considering that a volumetric strain of 10% is achieved upon pore collapse), in line with previous findings (e.g., *Sternlof et al.* [2005] adopted a ratio of band to undisturbed material bulk moduli equal to 1.5). It can be noticed that in this case, the reflected wave does not carry a net effective stress increase but a small decrease. This implies that the propagation of elastic waves through historic

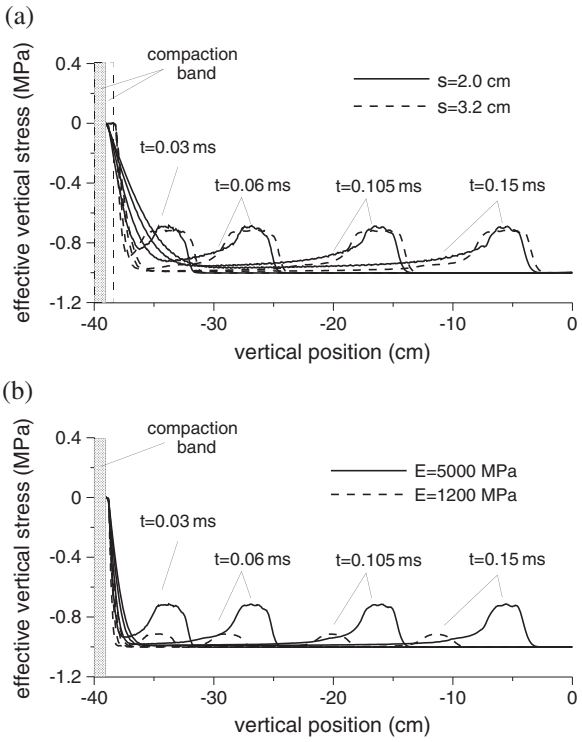

Figure 15. Effect of (a) CB thickness and of (b) the undisturbed stiffness in the shape of elastic waves. Figure 15a shows solid lines that represent waves generated by a 2 cm thick band, dashed lines represent waves generated by a 3.2 cm thick band. Figure 15b shows solid lines that are relevant to a material with $E = 5000$ MPa, dashed lines are relevant to a material with $E = 1200$ MPa. The CB stiffness decay function is the same as in Figure 2.

CBs, and, more in general, through a stiffer interface, is not bound to trigger further CB formation. A number of simulations were performed with different values of E_2/E_1, confirming the result that whenever $E_2/E_1 > 1$ no CB-genic reflections occur.

In Figure 15a the effect of CB thickness in the shape of the generated elastic waves is shown. By increasing the CB's thickness as an example from 2 cm to 3.2 cm, the resulting elastic wave shows little change, with slightly decreased amplitude and slightly increased duration of the pulse (corresponding to an increased horizontal breadth in the figure). This is not expected to substantially affect the reflected waves, hence the capability of promoting further CB generation. It can be also observed that the wave spatial breadth (corresponding to the wavelength of the overstress wave) is of the same order, or slightly larger, than the CB thickness (corresponding to the internal length scale of the material).

Figure 15b shows the impact of the undisturbed material's elastic modulus E in the shape of the elastic wave that is, as in the above discussed cases, generated from a sudden decay of stiffness within a 2 cm thick zone ($E_{CB}/E = 0.001$). It can be seen that waves propagating in a softer material (dashed line, $E = 1200$ MPa) are slightly slower and exhibit a much smaller amplitude, hence they are less effective, than those generated in a stiffer material (solid line, $E = 5000$ MPa). It follows that for the same material, the larger is its depth (i.e., the larger the confining stress, associated with increased stiffness in uncemented materials), the more bound dynamical induction of CBs is to occur. On the other hand, for materials located at the same depth, CBs are more likely to dynamically proliferate in stiffer materials (due to a slight cementation) compared to softer ones.

It is worth recalling that all the above considerations pertain to a post inception analysis, i.e., the analysis of subsequent CB formation after a first CB occurrence. The conditions under which a first CB is generated are disregarded. For this reason, the parameters involved in the analysis are not, in general, expected to play the same role in promoting cascade CB formation as in triggering a first CB.

The stiffness decay function adopted for all the above discussed simulations was shown in Figure 2, where the elastic modulus E was decreased to a final value $E_{CB} = E/1000$ in a total time $\Delta t = 15$ μs. The impact of the particular stiffness decay function on the generated wave shape was finally explored, by performing simulations on the one hand employing different values of final stiffness E_{CB}, on the other hand employing different values of decay time Δt. If the final stiffness of the decay function is reduced from $E_{CB} = E/1000$ to $E_{CB} = E/2000$ (keeping $\Delta t = 15$ μs for both cases), a slight reduction of horizontal breadth of the wave can be observed. If on the other hand the decay time is increased from 15 μs to 45 μs (keeping $E_{CB} = E/1000$ for both cases), a change of shape of the wave front brings about a moderate, but not substantial, wave amplitude reduction. For the sake of brevity, the relevant figures are omitted, but it can be observed that our results are substantially independent of the particular choice of stiffness decay function.

In light of the above outlined features, it is worth observing that while our analysis is suitable for interpreting in situ CB propagation, it cannot be readily applied to the reproduction of laboratory conditions. In fact, CBs in

laboratory sandstone samples (i) are usually associated with extensive grain crushing [*Baud et al*., 2004], (ii) are initiated as short discrete features that are arrested before propagating across the whole sample, sometimes leading to a mosaic of diffuse bands [*Baud et al*., 2004]; and (iii) often propagate from the end to the center of the specimen, progressively filling the sample [*Chemenda*, 2009]. These features do not always correspond to those observed in situ, where CBs are likely to form at modest burial and tectonic stresses, mostly in uncemented sand [*Holcomb et al*., 2007]. Moreover, the laboratory end platens, constituting a stiffer interface, do not appear appropriate to generate CB-genic wave reflections in the frame of our analysis (Figure 14). Finally, CB sets in laboratory samples are usually induced by a constant strain rate, in contrast with in situ conditions, that may possibly involve a constant stress state. Thus, it can be inferred that the propagation of CB sets in situ and in the laboratory may be governed by different mechanisms.

6. Conclusions

In this paper, an interpretation is proposed for the observed in situ occurrence of CBs according to a spatial distribution pattern, which is regulated by the material properties and by the geometry of the considered domain. Contrary to the majority of publications available, our analysis is focused on the dynamics of postlocalization regime, rather than on CB triggering mechanisms.

It is shown that after a first CB formation in an otherwise homogeneous sandy material (a phenomenon that has been widely investigated in the literature), subsequent CBs can occur due to the dynamical effects induced by the first CB. Elastic waves that are generated upon the sudden volumetric collapse involved in the formation of a CB, when reflected at the interface with a softer material or with a previously formed CB, produce significant local effective stress concentrations. These can promote further compaction localization in a cascade fashion, according to a regular pattern. The formation mechanism of subsequent CBs will end as soon as the spacing between the CBs is fine enough, depending on the permeability of the material (the smaller the hydraulic conductivity, the finer the expected limit CB spacing).

The spatial pattern of cascade-formed CBs is shown to depend on the domain geometry, namely, on the ratio α of the total domain length to the distance L of the first CB location from one of the domain boundaries. If α is an integer number, the CB distribution is homogeneous and the maximum number of CBs that can form equals $\alpha - 1$. If α is a rational number, the CB formation pattern is centrally symmetric, if the integer part of α is an odd number and its decimal part is smaller or equal to 0.5, and asymmetric otherwise.

The material properties promoting the in situ dynamical CB formation mechanism were also identified. A key factor in this sense is the in situ presence of intercalations of softer materials, as elastic waves are reflected with larger amplitude (carrying a CB-genic effective stress increase) upon crossing the interface with increasingly softer materials, while their reflection is unfruitful when they cross a stiffer material (such as an old compacted zone). On the other hand, encountering a permeability discontinuity for the elastic wave is not per se (if no significant excess pore pressure exist) a condition that induces fruitful reflections, as the high-frequency wave components are expected to mostly fade out before meeting any interface (for the range of permeability that is meaningful in this phenomenon). Further, a permeability range is likely to exist within which cascade CB formation is facilitated, as a very large permeability would inhibit the overstressing effect of reflected waves and a very small permeability would correspond to unsuitable mechanical characteristics for CB onset.

Another factor that enhances the amplitude of elastic waves, hence the possibility to promote CB formation is the overall stiffness of the layer, which is an increasing function of depth (for uncemented soils). It is therefore expected that deeper layers, all other things being equal, be more bound to experience dynamic CB-genic phenomena.

The above considerations are relevant to a post inception analysis, which disregards the conditions under which a first CB is generated. Hence, the involved parameters are not, in general, expected to play the same role in promoting cascade CB formation as in triggering a first CB.

The analysis proposed in this paper is aimed at constituting a stimulating starting point for further development and discussion in the geophysical community, as the model features and outcomes hereby outlined can be relatively easily checked against field data and possibly integrated with other types of analysis.

Table A1. List of the Main Parameter Values Employed in the Simulations

Parameter	Symbol	Value (or Range)	Units
Density of pore water	ρ_w	1000	Kg/m^3
Density of solid grains	ρ_s	2700	Kg/m^3
Poisson ratio of solid skeleton	ν	0.3	-
Elastic modulus of solid skeleton	E	1–5	GPa
Undisturbed porosity	n_0	0.25	-
Tortuosity	τ	1.5	-
Bulk modulus of pore water	K_w	2.18	GPa
Bulk modulus of solid grains	K_s	36	GPa

Appendix A

In sections A1–A3 the field equations on which the simulations are based are briefly described. The numerical solution of these equations is described in detail in *Gajo and Denzer* [2011], to which the interested reader is referred for further details. Table A1 is reported showing relevant parameter values employed in our calculations.

A1. Fluid Mass Balance

Let us first define the variation of fluid mass content per unit volume of the undeformed solid skeleton $\overline{m}_w$ as the difference between the current fluid mass content m_w and the initial fluid mass content m_{w0}

$$\overline{m}_w = m_w - m_{w0} = \rho_w n \boldsymbol{J} - \rho_{w0} n_0 \tag{A1}$$

where ρ_w and ρ_{w0} the current and initial density of the pore fluid, n and n_0 the current and initial porosity, and $\boldsymbol{J}$ the Jacobian of the deformation gradient.

The rate of variation of fluid mass content in the reference configuration is expressed as

$$\dot{\overline{m}}_w = -\mathrm{Div}\mathbf{M}_R \tag{A2}$$

where $\mathbf{M}_R$ is the so-called Piola-Kirchoff mass flux in the reference configuration. For a hydraulically isotropic porous material, $\mathbf{M}_R$ can be expressed according to Darcy's law as

$$\mathbf{M}_R = -\rho_w \frac{K_D^0}{g} \mathrm{Grad}(\mu_w + U) \tag{A3}$$

In the above, g is the gravity acceleration, K_D^0 the hydraulic conductivity in the reference configuration, U the body force potential per unit mass, and μ_w the chemical potential. The latter represents the free energy per unit mass of pore fluid and is univocally related to pore pressure p_w through the expression $\dot{\mu}_w = \dot{p}_w/\rho_w$.

A2. Momentum Balance for the Whole Porous Medium

For a volume element moving with the solid phase, the momentum balance equation for the whole porous medium in the reference configuration can be written as

$$\overbrace{(1-n_0)\rho_{s0}\ddot{\mathbf{x}} + [n\rho_w \boldsymbol{J}(\dot{\mathbf{x}} + \overline{\boldsymbol{w}})]}^{(1)} = \overbrace{-\mathrm{Div}[(\dot{\mathbf{x}} + \overline{\boldsymbol{w}}) \otimes \mathbf{M}_R]}^{(2)} + \\ + \overbrace{\mathrm{Div}\mathbf{S}}^{(3)} + \overbrace{[(1-n_0)\rho_{s0} + n\rho_w \boldsymbol{J}]\mathbf{b}_0}^{(4)} \tag{A4}$$

where ρ_{s0} the initial density of the solid phase, $\dot{\mathbf{x}}$ and $\ddot{\mathbf{x}}$, respectively, the material description of the velocity and acceleration of the solid phase, $\overline{\boldsymbol{w}}$ the spatial description of the relative velocity of the fluid phase with respect to the solid phase, $\mathbf{S}$ the total first *Piola–Kirchhoff* stress tensor, and $\mathbf{b}_0 = -\mathrm{Grad}U$ the body force per unit mass in the reference configuration.

The physical meaning of the different terms featuring in equation (A4) can be stated as follows: (1) rate of increase in momentum per unit undeformed volume, (2) rate of momentum gain by convection per unit undeformed volume, (3) traction forces on the infinitesimal porous volume per unit undeformed volume, and (4) gravitational forces on the infinitesimal porous volume per unit undeformed volume.

A3. Momentum Balance for the Pore Fluid

For a volume element moving with the solid phase the momentum balance equation for the pore fluid in the reference configuration can be expressed as

$$n\rho_w \boldsymbol{J}\left(\dot{\mathbf{x}}+\dot{\overline{\boldsymbol{w}}}\right)=-n\rho_w \boldsymbol{J}\left(\dot{\mathbf{F}}+\mathrm{Grad}\dot{\overline{w}}\right)\mathbf{F}^{-1}\overline{\boldsymbol{w}}+n\mathrm{Div}\left(-\boldsymbol{J}p_w\mathbf{F}^{-T}\right)+ \\ +f_{w0}+n\rho_w \boldsymbol{J}\mathbf{b_0} \tag{A5}$$

In the above, **F** is the deformation gradient, and the quantity

$$f_{w0}=-n\boldsymbol{J}^2\frac{g}{\mathbf{K}_D^0}\left(\frac{1}{\boldsymbol{J}}\mathbf{F}^{-T}\mathbf{M}_R\right)-\boldsymbol{J}\rho_a\dot{\overline{\boldsymbol{w}}} \tag{A6}$$

is termed *momentum supply*, as it denotes the momentum supplied by the solid phase to the fluid phase, where ρ_a is the virtual mass per unit of deformed volume of saturated porous medium. In the literature, the virtual mass is usually expressed as

$$\rho_a=(\tau-1)n\rho_w \tag{A7}$$

where τ is the tortuosity that can be estimated from the porosity using empirical relationships or theoretical analyses [*Gajo*, 1996].

Acknowledgments
The authors gratefully acknowledge financial support from European Union FP7 project under contract PIAPP-GA-2013-609758-HOTBRICKS. Data files for this paper shall be made available in the institutional archive of the University of Trento (http://eprints.biblio.unitn.it).

References

Baud, P., E. Klein, and T. Wong (2004), Compaction localization in porous sandstones: Spatial evolution of damage and acoustic emission activity, *J. Struct. Geol.*, *26*(4), 603–624, doi:10.1016/j.jsg.2003.09.002.
Bigoni, D., and D. Zaccaria (1992), Strong ellipticity of comparison solids in elastoplasticity with volumetric non-associativity, *Int. J. Solids Struct.*, *29*, 2123–2136.
Biot, M. A. (1941), A general theory of three-dimensional consolidation, *J. Appl. Phys.*, *12*, 155–164.
Biot, M. A. (1956), Theory of propagation of elastic waves in a fluid saturated porous solid, *J. Acoust. Soc. Am.*, *28*, 168–191.
Biot, M. A. (1962a), Mechanics of deformation and acoustic propagation in porous media, *J. Appl. Phys.*, *27*, 459–467.
Biot, M. A. (1962b), Generalized theory of acoustic propagation in porous dissipation media, *J. Acoust. Soc. Am.*, *34*, 1254–1264.
Biot, M. A. (1973), Nonlinear and semilinear rheology of porous media, *J. Geophys. Res.*, *78*, 4924–4937, doi:10.1029/JB078i023p04924.
Bourbié, T., O. Coussy, and B. Zinszner (1987), *Acoustics of Porous Media*, Editions Technip, Paris, France.
Castellanza, R., E. Gerolymatou, and R. Nova (2009), Experimental observations and modelling of compaction bands in oedometric tests on high porosity rocks, *Strain*, *45*, 410–423.
Chemenda, A. I. (2009), The formation of tabular compaction-band arrays: Theoretical and numerical analysis, *J. Mech. Phys. Solids*, *57*, 851–868.
De Meer, S. D., C. Spiers, and C. Peach (2000), Kinetics of precipitation of gypsum and implications for pressure-solution creep, *J. Geol. Soc. London*, *157*, 269–281.
Fletcher, R. C., and D. D. Pollard (1981), Anticrack model for pressure solution surfaces, *Geology*, *9*(9), 419–424.
Fossen, H., R. A. Schultz, and A. Torabi (2011), Conditions and implications for compaction band formation in the Navajo Sandstone, Utah, *J. Struct. Geol.*, *33*(10), 1477–1490.
Gajo, A. (1995), Influence of viscous coupling in propagation of elastic waves in saturated soil, *J. Geotech. Eng.*, *121*(9), 636–644.
Gajo, A. (1996), The effects of inertial coupling in the interpretation of dynamic soil tests, *Geotechnique*, *46*(2), 245–257.
Gajo, A. (2010), A general approach to isothermal hyperelastic modelling of saturated porous media at finite strains with compressible solid constituents, *Proc. R. Soc. A*, *466*(2122), 3061–3087.
Gajo, A., and R. Denzer (2011), Finite element modelling of saturated porous media at finite strains under dynamic conditions with compressible constituents, *Int. J. Numer. Methods Eng.*, *85*, 1705–1736.
Gajo, A., D. Bigoni, and D. Muir Wood (2004), Multiple shear band development and related instabilities in granular materials, *J. Mech. Phys. Solids*, *52*, 2683–2724.
Haimson, B. C., and I. Song (1998), Mechanics of rock fracturing around boreholes, in *Mechanics of Jointed and Faulted Rock*, edited by Rossmanith, pp. 325–330, A. A. Balkema, Rotterdam.
Hardin, B. O., and W. L. Black (1968), Vibration modulus of normally consolidated clay, *J. Soil Mech. Found. Div., Am. Soc. Civ. Eng.*, *94*(SM2), 353–369.
Holcomb, D. J., and W. A. Olsson (2003), Compaction localization and fluid flow, *J. Geophys. Res.*, *108*(B6), 2290, doi:10.1029/2001JB000813.
Holcomb, D., J. Rudnicki, K. Issen, and K. Sternlof (2007), Compaction localization in the Earth and the laboratory: State of the research and research directions, *Acta Geotech.*, *2*, 1–15.
Issen, K. A., and J. W. Rudnicki (2000), Conditions for compaction bands in porous rock, *J. Geophys. Res.*, *105*, 21,529–21,536, doi:10.1029/2000JB900185.
Katsman, R., E. Aharonov, and B. C. Haimson (2009), Compaction bands induced by borehole drilling, *Acta Geotech.*, *4*(3), 151–162.
Klein, E., P. Baud, T. Reuschlé, and T. F. Wong (2001), Mechanical behaviour and failure mode of Bentheim sandstone under triaxial compression, *Phys. Chem. Earth Part A*, *26*(1), 21–25.
Lajtai, E. Z. (1974), Brittle fracture in compression, *Int. J. Fract.*, *10*(4), 525–536.
Mollema, P., and M. Antonellini (1996), Compaction bands: A structural analog for anti-mode i cracks in aeolian sandstone, *Tectonophysics*, *267*, 209–228.
Nova, R., R. Castellanza, and C. Tamagnini (2003), A constitutive model for bonded geomaterials subject to mechanical and/or chemical degradation, *Int. J. Numer. Anal. Methods Geomech.*, *27*, 705–732.
Oka, F., S. Kimoto, Y. Higo, H. Ohta, T. Sanagawa, and T. Kodaka (2011), An elasto-viscoplastic model for diatomaceous mudstone and numerical simulation of compaction bands, *Int. J. Numer. Anal. Methods Geomech.*, *35*, 244–263.

Olsson, W. (1999), Theoretical and experimental investigation of compaction bands in porous rock, *J. Geophys. Res.*, *104*(B4), 7219–7228, doi:10.1029/1998JB900120.

Olsson, W. A. (2001), Quasistatic propagation of compaction fronts in porous rock, *Mech. Mater.*, *33*(11), 659–668.

Regenauer-Lieb, K., M. Veveakis, T. Poulet, F. Wellmann, A. Karrech, J. Liu, J. Hauser, C. Schrank, O. Gaede, and M. Trefry (2013), Multiscale coupling and multiphysics approaches in Earth sciences: Theory, *J. Coupled Syst. Multiscale Dyn.*, *1*, doi:10.1166/jcsmd.2013.1021.

Rice, J. R., and J. W. Rudnicki (1980), A note on some features of the theory of localization of deformation, *Int. J. Solids Struct.*, *16*, 597–605.

Rudnicki, J. W., and J. R. Rice (1975), Conditions for the localization of deformation in pressure-sensitive dilatant materials, *J. Mech. Phys. Solids*, *23*, 371–394.

Schultz, R. (2009), Scaling and paleodepth of compaction bands, Nevada and Utah, *J. Geophys. Res.*, *114*, B03407, doi:10.1029/2008JB005876.

Stefanou, I., and J. Sulem (2014), Chemically induced compaction bands: Triggering conditions and band thickness, *J. Geophys. Res. Solid Earth*, *119*, 880–899, doi:10.1002/2013JB010342.

Sternlof, K., J. W. Rudnicki, and D. D. Pollard (2005), Anticrack-inclusion model for compaction bands in sandstone, *J. Geophys. Res.*, *110*, B11463, doi:10.1029/2005JB0037664.

Sternolf, K. R. (2006), Structural geology, propagation mechanics and hydraulic effects of compaction bands in sandstone, PhD thesis, Stanford Univ., Palo Alto, Calif.